Research Article | Vol. 8, No. 2 | 1 Feb 2017 | BIOMEDICAL OPTICS EXPRESS 1221

Biomedical Optics EXPRESS

Ultrahigh-resolution OCT imaging of the human cornea

RENÉ M. WERKMEISTER,[1,2] SABINA SAPETA,[1,3] DOREEN SCHMIDL,[4] GERHARD GARHÖFER,[2,4] GERALD SCHMIDINGER,[5] VALENTIN ARANHA DOS SANTOS,[1] GEROLD C. ASCHINGER,[1] ISABELLA BAUMGARTNER,[5] NIKLAS PIRCHER,[5] FLORIAN SCHWARZHANS,[5,6] ANCA PANTALON,[7] HARMINDER DUA,[8] AND LEOPOLD SCHMETTERER[1,2,3,4,9,*]

[1]*Center for Medical Physics and Biomedical Engineering, Medical University of Vienna, Waehringer Guertel 18-20, A-1090 Vienna, Austria*
[2]*Christian Doppler Laboratory for Ocular and Dermal Effects of Thiomers, Medical University of Vienna, Waehringer Guertel 18-20, A-1090 Vienna, Austria*
[3]*Singapore Eye Research Institute The Academia, 20 College Road, Discovery Tower Level 6, 169856, Singapore*
[4]*Department of Clinical Pharmacology, Medical University of Vienna, Waehringer Guertel 18-20, A-1090 Vienna, Austria*
[5]*Department of Ophthalmology, Medical University of Vienna, Waehringer Guertel 18-20, A-1090 Vienna, Austria*
[6]*Center for Medical Statistics, Informatics and Intelligent Systems, Medical University of Vienna, Spitalgasse 23, A-1090 Vienna, Austria*
[7]*Department of Ophthalmology, Gr. T. Popa University of Medicine and Pharmacy, Iasi, Sf. Spiridon University Hospital, 16 Universitatii Str, Iasi, 700115, Romania*
[8]*Academic Section of Ophthalmology, Division of Clinical Neuroscience, Nottingham University Hospitals NHS Trust QMC campus, Derby Road, Nottingham, NG7 2UH, UK*
[9]*Lee Kong Chian School of Medicine, Nanyang Technological University Novena Campus, 11 Mandalay Road, 308232, Singapore*
[*]*leopold.schmetterer@meduniwien.ac.at*

Abstract: We present imaging of corneal pathologies using optical coherence tomography (OCT) with high resolution. To this end, an ultrahigh-resolution spectral domain OCT (UHR-OCT) system based on a broad bandwidth Ti:sapphire laser is employed. With a central wavelength of 800 nm, the imaging device allows to acquire OCT data at the central, paracentral and peripheral cornea as well as the limbal region with 1.2 µm x 20 µm (axial x lateral) resolution at a rate of 140 000 A-scans/s. Structures of the anterior segment of the eye, not accessible with commercial OCT systems, are visualized. These include corneal nerves, limbal palisades of Vogt as well as several corneal pathologies. Cases such as keratoconus and Fuchs's endothelial dystrophy as well as infectious changes caused by diseases like Acanthamoeba keratitis and scarring after herpetic keratitis are presented. We also demonstrate the applicability of our system to visualize epithelial erosion and intracorneal foreign body after corneal trauma as well as chemical burns. Finally, results after Descemet's membrane endothelial keratoplasty (DMEK) are imaged. These clinical cases show the potential of UHR-OCT to help in clinical decision-making and follow-up. Our results and experience indicate that UHR-OCT of the cornea is a promising technique for the use in clinical practice, but can also help to gain novel insight in the physiology and pathophysiology of the human cornea.

OCIS codes: (170.0110) Imaging systems; (170.4460) Ophthalmic optics and devices; (170.4500) Optical coherence tomography.

#280295 https://doi.org/10.1364/BOE.8.001221
Journal © 2017 Received 7 Nov 2016; revised 19 Dec 2016; accepted 26 Dec 2016; published 30 Jan 2017

Biomedical Optics EXPRESS

References and links

1. J. P. Whitcher, M. Srinivasan, and M. P. Upadhyay, "Corneal blindness: a global perspective," Bull. World Health Organ. **79**(3), 214–221 (2001).
2. G. K. Klintworth, "Corneal dystrophies," Orphanet J. Rare Dis. **4**(1), 7 (2009).
3. M. W. Belin and S. S. Khachikian, "An introduction to understanding elevation-based topography: how elevation data are displayed - a review," Clin. Experiment. Ophthalmol. **37**(1), 14–29 (2009).
4. G. Cairns and C. N. McGhee, "Orbscan computerized topography: attributes, applications, and limitations," J. Cataract Refract. Surg. **31**(1), 205–220 (2005).
5. P. Rosales and S. Marcos, "Pentacam Scheimpflug quantitative imaging of the crystalline lens and intraocular lens," J. Refract. Surg. **25**(5), 421–428 (2009).
6. D. Z. Reinstein, R. H. Silverman, T. Raevsky, G. J. Simoni, H. O. Lloyd, D. J. Najafi, M. J. Rondeau, and D. J. Coleman, "Arc-scanning very high-frequency digital ultrasound for 3D pachymetric mapping of the corneal epithelium and stroma in laser in situ keratomileusis," J. Refract. Surg. **16**(4), 414–430 (2000).
7. B. E. McCarey, H. F. Edelhauser, and M. J. Lynn, "Review of corneal endothelial specular microscopy for FDA clinical trials of refractive procedures, surgical devices, and new intraocular drugs and solutions," Cornea **27**(1), 1–16 (2008).
8. R. F. Guthoff, A. Zhivov, and O. Stachs, "In vivo confocal microscopy, an inner vision of the cornea - a major review," Clin. Experiment. Ophthalmol. **37**(1), 100–117 (2009).
9. E. A. Swanson, J. A. Izatt, M. R. Hee, D. Huang, C. P. Lin, J. S. Schuman, C. A. Puliafito, and J. G. Fujimoto, "In vivo retinal imaging by optical coherence tomography," Opt. Lett. **18**(21), 1864–1866 (1993).
10. J. A. Izatt, M. R. Hee, E. A. Swanson, C. P. Lin, D. Huang, J. S. Schuman, C. A. Puliafito, and J. G. Fujimoto, "Micrometer-scale resolution imaging of the anterior eye in vivo with optical coherence tomography," Arch. Ophthalmol. **112**(12), 1584–1589 (1994).
11. P. Li, L. An, R. Reif, T. T. Shen, M. Johnstone, and R. K. Wang, "In vivo microstructural and microvascular imaging of the human corneo-scleral limbus using optical coherence tomography," Biomed. Opt. Express **2**(11), 3109–3118 (2011).
12. Y. Yasuno, V. D. Madjarova, S. Makita, M. Akiba, A. Morosawa, C. Chong, T. Sakai, K. P. Chan, M. Itoh, and T. Yatagai, "Three-dimensional and high-speed swept-source optical coherence tomography for in vivo investigation of human anterior eye segments," Opt. Express **13**(26), 10652–10664 (2005).
13. M. Gora, K. Karnowski, M. Szkulmowski, B. J. Kaluzny, R. Huber, A. Kowalczyk, and M. Wojtkowski, "Ultra high-speed swept source OCT imaging of the anterior segment of human eye at 200 kHz with adjustable imaging range," Opt. Express **17**(17), 14880–14894 (2009).
14. I. Grulkowski, J. J. Liu, B. Baumann, B. Potsaid, C. Lu, and J. G. Fujimoto, "Imaging limbal and scleral vasculature using Swept Source Optical Coherence Tomography," Photonics Lett. Pol. **3**(4), 132–134 (2011).
15. M. Ruggeri, S. R. Uhlhorn, C. De Freitas, A. Ho, F. Manns, and J. M. Parel, "Imaging and full-length biometry of the eye during accommodation using spectral domain OCT with an optical switch," Biomed. Opt. Express **3**(7), 1506–1520 (2012).
16. K. Grieve, M. Paques, A. Dubois, J. Sahel, C. Boccara, and J. F. Le Gargasson, "Ocular tissue imaging using ultrahigh-resolution, full-field optical coherence tomography," Invest. Ophthalmol. Vis. Sci. **45**(11), 4126–4131 (2004).
17. V. Christopoulos, L. Kagemann, G. Wollstein, H. Ishikawa, M. L. Gabriele, M. Wojtkowski, V. Srinivasan, J. G. Fujimoto, J. S. Duker, D. K. Dhaliwal, and J. S. Schuman, "In vivo corneal high-speed, ultra high-resolution optical coherence tomography," Arch. Ophthalmol. **125**(8), 1027–1035 (2007).
18. R. Yadav, K. S. Lee, J. P. Rolland, J. M. Zavislan, J. V. Aquavella, and G. Yoon, "Micrometer axial resolution OCT for corneal imaging," Biomed. Opt. Express **2**(11), 3037–3046 (2011).
19. B. J. Kaluzny, M. Gora, K. Karnowski, I. Grulkowski, A. Kowalczyk, and M. Wojtkowski, "Imaging of the lens capsule with an ultrahigh-resolution spectral optical coherence tomography prototype based on a femtosecond laser," Br. J. Ophthalmol. **94**(3), 275–277 (2010).
20. L. Kagemann, G. Wollstein, H. Ishikawa, Z. Nadler, I. A. Sigal, L. S. Folio, and J. S. Schuman, "Visualization of the conventional outflow pathway in the living human eye," Ophthalmology **119**(8), 1563–1568 (2012).
21. L. Kagemann, G. Wollstein, H. Ishikawa, R. A. Bilonick, P. M. Brennen, L. S. Folio, M. L. Gabriele, and J. S. Schuman, "Identification and assessment of Schlemm's canal by spectral-domain optical coherence tomography," Invest. Ophthalmol. Vis. Sci. **51**(8), 4054–4059 (2010).
22. K. Grieve, D. Ghoubay, C. Georgeon, O. Thouvenin, N. Bouheraoua, M. Paques, and V. M. Borderie, "Three-dimensional structure of the mammalian limbal stem cell niche," Exp. Eye Res. **140**, 75–84 (2015).
23. K. L. Lathrop, D. Gupta, L. Kagemann, J. S. Schuman, and N. Sundarraj, "Optical coherence tomography as a rapid, accurate, noncontact method of visualizing the palisades of Vogt," Invest. Ophthalmol. Vis. Sci. **53**(3), 1381–1387 (2012).
24. K. Bizheva, N. Hutchings, L. Sorbara, A. A. Moayed, and T. Simpson, "In vivo volumetric imaging of the human corneo-scleral limbus with spectral domain OCT," Biomed. Opt. Express **2**(7), 1794–1802 (2011).
25. Y. Li, O. Tan, R. Brass, J. L. Weiss, and D. Huang, "Corneal epithelial thickness mapping by Fourier-domain optical coherence tomography in normal and keratoconic eyes," Ophthalmology **119**(12), 2425–2433 (2012).

Biomedical Optics EXPRESS

26. R. Yadav, R. Kottaiyan, K. Ahmad, and G. Yoon, "Epithelium and Bowman's layer thickness and light scatter in keratoconic cornea evaluated using ultrahigh resolution optical coherence tomography," J. Biomed. Opt. **17**(11), 116010 (2012).
27. M. A. Shousha, V. L. Perez, J. Wang, T. Ide, S. Jiao, Q. Chen, V. Chang, N. Buchser, S. R. Dubovy, W. Feuer, and S. H. Yoo, "Use of ultra-high-resolution optical coherence tomography to detect in vivo characteristics of Descemet's membrane in Fuchs' dystrophy," Ophthalmology **117**(6), 1220–1227 (2010).
28. B. J. Kaluzny, A. Szkulmowska, M. Szkulmowski, T. Bajraszewski, A. Kowalczyk, and M. Wojtkowski, "Fuchs' endothelial dystrophy in 830-nm spectral domain optical coherence tomography," Ophthalmic Surg. Lasers Imaging **40**(2), 198–200 (2009).
29. W. Drexler and J. G. Fujimoto, "Introduction to Optical Coherence Tomography," in *Optical Coherence Tomography*, W. Drexler and J. G. Fujimoto, eds. (Springer, Berlin Heidelberg New York, 2008), pp. 1–40.
30. S. Murali, K. P. Thompson, and J. P. Rolland, "Three-dimensional adaptive microscopy using embedded liquid lens," Opt. Lett. **34**(2), 145–147 (2009).
31. P. Tankam, Z. He, Y. J. Chu, J. Won, C. Canavesi, T. Lepine, H. B. Hindman, D. J. Topham, P. Gain, G. Thuret, and J. P. Rolland, "Assessing microstructures of the cornea with Gabor-domain optical coherence microscopy: pathway for corneal physiology and diseases," Opt. Lett. **40**(6), 1113–1116 (2015).
32. S. W. Rush, D. Y. Han, and R. B. Rush, "Optical coherence tomography-guided transepithelial phototherapeutic keratectomy for the treatment of anterior corneal scarring," Am. J. Ophthalmol. **156**(6), 1088–1094 (2013).
33. B. J. Kaluzny, M. Szkulmowski, D. M. Bukowska, and M. Wojtkowski, "Spectral OCT with speckle contrast reduction for evaluation of the healing process after PRK and transepithelial PRK," Biomed. Opt. Express **5**(4), 1089–1098 (2014).
34. A. M. Bata, K. J. Witkowska, P. A. Wozniak, K. Fondi, G. Schmidinger, N. Pircher, S. Szegedi, V. Aranha Dos Santos, A. Pantalon, R. M. Werkmeister, G. Garhofer, L. Schmetterer, and D. Schmidl, "Effect of a Matrix Therapy Agent on Corneal Epithelial Healing After Standard Collagen Cross-linking in Patients With Keratoconus: A Randomized Clinical Trial," JAMA Ophthalmol. **134**(10), 1169–1176 (2016).
35. R. M. Werkmeister, A. Alex, S. Kaya, A. Unterhuber, B. Hofer, J. Riedl, M. Bronhagl, M. Vietauer, D. Schmidl, T. Schmoll, G. Garhöfer, W. Drexler, R. A. Leitgeb, M. Groeschl, and L. Schmetterer, "Measurement of tear film thickness using ultrahigh-resolution optical coherence tomography," Invest. Ophthalmol. Vis. Sci. **54**(8), 5578–5583 (2013).
36. T. Schmoll, A. Unterhuber, C. Kolbitsch, T. Le, A. Stingl, and R. Leitgeb, "Precise thickness measurements of Bowman's layer, epithelium, and tear film," Optom. Vis. Sci. **89**(5), E795–E802 (2012).
37. V. Aranha Dos Santos, L. Schmetterer, M. Gröschl, G. Garhofer, D. Schmidl, M. Kucera, A. Unterhuber, J. P. Hermand, and R. M. Werkmeister, "In vivo tear film thickness measurement and tear film dynamics visualization using spectral domain optical coherence tomography," Opt. Express **23**(16), 21043–21063 (2015).
38. D. Schmidl, K. J. Witkowska, S. Kaya, C. Baar, H. Faatz, J. Nepp, A. Unterhuber, R. M. Werkmeister, G. Garhofer, and L. Schmetterer, "The association between subjective and objective parameters for the assessment of dry-eye syndrome," Invest. Ophthalmol. Vis. Sci. **56**(3), 1467–1472 (2015).
39. D. Schmidl, L. Schmetterer, K. J. Witkowska, A. Unterhuber, V. A. dos Santos, S. Kaya, J. Nepp, C. Baar, P. Rosner, R. M. Werkmeister, and G. Garhofer, "Tear Film Thickness After Treatment with Artificial Tears in Patients with Moderate Dry Eye Disease," Cornea **34**(4), 421–426 (2015).
40. V. A. Dos Santos, L. Schmetterer, G. J. Triggs, R. A. Leitgeb, M. Gröschl, A. Messner, D. Schmidl, G. Garhofer, G. Aschinger, and R. M. Werkmeister, "Super-resolved thickness maps of thin film phantoms and in vivo visualization of tear film lipid layer using OCT," Biomed. Opt. Express **7**(7), 2650–2670 (2016).
41. International Electrotechnical Commission, "International Electrotechnical Commission IEC 60825-1, Safety of laser products - Part 1: Equipment classification and requirements (IEC 60825-1:2014)," (2014).
42. American National Standards Institute, "American National Standard for Safe Use of Lasers. Orlando, FL: The Laser Institute of America; 2000. ANSI Z136.1-2014," (2014).
43. P. Thévenaz, U. E. Ruttimann, and M. Unser, "A pyramid approach to subpixel registration based on intensity," IEEE Trans. Image Process. **7**(1), 27–41 (1998).
44. V. V. Tuchin, *Optical Clearing of Tissue and Blood* (SPIE Publications, 2005).
45. S. Patel, J. Marshall, and F. W. Fitzke 3rd, "Refractive index of the human corneal epithelium and stroma," J. Refract. Surg. **11**(2), 100–105 (1995).
46. Z. Chen, C. S. de Paiva, L. Luo, F. L. Kretzer, S. C. Pflugfelder, and D. Q. Li, "Characterization of putative stem cell phenotype in human limbal epithelia," Stem Cells **22**(3), 355–366 (2004).
47. M. J. German, H. M. Pollock, B. Zhao, M. J. Tobin, A. Hammiche, A. Bentley, L. J. Cooper, F. L. Martin, and N. J. Fullwood, "Characterization of putative stem cell populations in the cornea using synchrotron infrared microspectroscopy," Invest. Ophthalmol. Vis. Sci. **47**(6), 2417–2421 (2006).
48. I. Jalbert, F. Stapleton, E. Papas, D. F. Sweeney, and M. Coroneo, "In vivo confocal microscopy of the human cornea," Br. J. Ophthalmol. **87**(2), 225–236 (2003).
49. A. G. Chiou, S. C. Kaufman, H. E. Kaufman, and R. W. Beuerman, "Clinical corneal confocal microscopy," Surv. Ophthalmol. **51**(5), 482–500 (2006).
50. N. Takahashi, T. Chikama, R. Yanai, and T. Nishida, "Structures of the corneal limbus detected by laser-scanning confocal biomicroscopy as related to the palisades of Vogt detected by slit-lamp microscopy," Jpn. J. Ophthalmol. **53**(3), 199–203 (2009).
51. M. F. Goldberg and A. J. Bron, "Limbal palisades of Vogt," Trans. Am. Ophthalmol. Soc. **80**, 155–171 (1982).

Biomedical Optics EXPRESS

52. L. J. Müller, C. F. Marfurt, F. Kruse, and T. M. Tervo, "Corneal nerves: structure, contents and function," Exp. Eye Res. **76**(5), 521–542 (2003).
53. Y. S. Rabinowitz, "Keratoconus," Surv. Ophthalmol. **42**(4), 297–319 (1998).
54. A. Gokul, D. V. Patel, G. A. Watters, and C. N. McGhee, "The natural history of corneal topographic progression of keratoconus after age 30 years in non-contact lens wearers," Br. J. Ophthalmol. **2016**, 308682 (2016).
55. G. Vedana, G. Villarreal, Jr., and A. S. Jun, "Fuchs endothelial corneal dystrophy: current perspectives," Clin. Ophthalmol. **10**, 321–330 (2016).
56. K. Bizheva, L. Haines, E. Mason, B. MacLellan, B. Tan, D. Hileeto, and L. Sorbara, "In Vivo Imaging and Morphometry of the Human Pre-Descemet's Layer and Endothelium With Ultrahigh-Resolution Optical Coherence Tomography," Invest. Ophthalmol. Vis. Sci. **57**(6), 2782–2787 (2016).
57. H. S. Dua, V. A. Shanmuganathan, A. O. Powell-Richards, P. J. Tighe, and A. Joseph, "Limbal epithelial crypts: a novel anatomical structure and a putative limbal stem cell niche," Br. J. Ophthalmol. **89**(5), 529–532 (2005).
58. V. A. Shanmuganathan, T. Foster, B. B. Kulkarni, A. Hopkinson, T. Gray, D. G. Powe, J. Lowe, and H. S. Dua, "Morphological characteristics of the limbal epithelial crypt," Br. J. Ophthalmol. **91**(4), 514–519 (2007).
59. K. Falke, R. K. Prakasam, R. F. Guthoff, and O. Stachs, "[In vivo imaging of limbal epithelium and palisades of Vogt]," Klin. Monatsbl. Augenheilkd. **229**(12), 1185–1190 (2012).
60. A. Cruzat, Y. Qazi, and P. Hamrah, "In vivo confocal microscopy of corneal nerves in health and disease," Ocul. Surf. **15**(1), 15–47 (2016).
61. B. Klenkler, H. Sheardown, and L. Jones, "Growth factors in the tear film: role in tissue maintenance, wound healing, and ocular pathology," Ocul. Surf. **5**(3), 228–239 (2007).
62. H. A. Al-Ghadeer and A. Al-Assiri, "Identification and localization of multiple intrastromal foreign bodies with anterior segment optical coherence tomography and ocular Pentacam," Int. Ophthalmol. **34**(2), 355–358 (2014).
63. L. N. Estrada and C. E. Rosenstiel, "RGP lens treats irregular astigmatism from intracorneal glass," Eye Contact Lens **29**(3), 193–194 (2003).
64. M. J. Mannis, C. E. Fiori, J. H. Krachmer, M. M. Rodrigues, and G. Pardos, "Keratopathy associated with intracorneal glass," Arch. Ophthalmol. **99**(5), 850–852 (1981).
65. N. Sharma, D. Singh, A. Sobti, P. Agarwal, T. Velpandian, J. S. Titiyal, and S. Ghose, "Course and outcome of accidental sodium hydroxide ocular injury," Am. J. Ophthalmol. **154**(4), 740–749 (2012).
66. G. A. Secker and J. T. Daniels, "Corneal epithelial stem cells: deficiency and regulation," Stem Cell Rev. **4**(3), 159–168 (2008).
67. V. S. Sangwan, S. Basu, S. MacNeil, and D. Balasubramanian, "Simple limbal epithelial transplantation (SLET): a novel surgical technique for the treatment of unilateral limbal stem cell deficiency," Br. J. Ophthalmol. **96**(7), 931–934 (2012).
68. S. K. Arya, A. Bhatti, A. Raj, and R. K. Bamotra, "Simple Limbal Epithelial Transplantation in Acid Injury and Severe Dry Eye," J. Clin. Diagn. Res. **10**(6), ND06–ND07 (2016).
69. A. Shiraishi, T. Kobayashi, Y. Hara, M. Yamaguchi, T. Uno, and Y. Ohashi, "Rapid detection of Acanthamoeba cysts in frozen sections of corneal scrapings with Fungiflora Y," Br. J. Ophthalmol. **93**(12), 1563–1565 (2009).
70. J. P. Essepian, R. K. Rajpal, D. T. Azar, K. New, R. Antonacci, W. Shields, and W. J. Stark, "The use of confocal microscopy in evaluating corneal wound healing after excimer laser keratectomy," Scanning **16**(5), 300–304 (1994).
71. K. Winchester, W. D. Mathers, J. E. Sutphin, and T. E. Daley, "Diagnosis of Acanthamoeba keratitis in vivo with confocal microscopy," Cornea **14**(1), 10–17 (1995).
72. D. R. Pfister, J. D. Cameron, J. H. Krachmer, and E. J. Holland, "Confocal microscopy findings of Acanthamoeba keratitis," Am. J. Ophthalmol. **121**(2), 119–128 (1996).
73. V. Chen-Espinoza, T. Nakamura, Y. Li, M. Trousdale, J. A. Irvine, and D. Huang, "High-Resolution Optical Coherence Tomography of Acanthamoeba Keratitis," in *Association for Research in Vision and Ophthalmology,* (Fort Lauderdale, Florida, 2008).
74. C. Wittig-Silva, E. Chan, F. M. Islam, T. Wu, M. Whiting, and G. R. Snibson, "A randomized, controlled trial of corneal collagen cross-linking in progressive keratoconus: three-year results," Ophthalmology **121**(4), 812–821 (2014).
75. L. Mastropasqua, "Collagen cross-linking: when and how? A review of the state of the art of the technique and new perspectives," Eye Vis (Lond) **2**(1), 19 (2015).
76. S. Catalan, L. Cadarso, F. Esteves, J. Salgado-Borges, M. Lopez, and C. Cadarso, "Assessment of Corneal Epithelial Thickness in Asymmetric Keratoconic Eyes and Normal Eyes Using Fourier Domain Optical Coherence Tomography," J. Ophthalmol. **2016**, 5697343 (2016).
77. C. Temstet, O. Sandali, N. Bouheraoua, T. Hamiche, A. Galan, M. El Sanharawi, E. Basli, L. Laroche, and V. Borderie, "Corneal epithelial thickness mapping using Fourier-domain optical coherence tomography for detection of form fruste keratoconus," J. Cataract Refract. Surg. **41**(4), 812–820 (2015).
78. G. K. Klintworth, "Corneal dystrophies," Orphanet J. Rare Dis. **4**(1), 7 (2009).
79. A. O. Eghrari, Y. J. Daoud, and J. D. Gottsch, "Cataract surgery in Fuchs corneal dystrophy," Curr. Opin. Ophthalmol. **21**(1), 15–19 (2010).
80. M. A. Nanavaty, X. Wang, and A. J. Shortt, "Endothelial keratoplasty versus penetrating keratoplasty for Fuchs endothelial dystrophy," Cochrane Database Syst. Rev. **2**(2), CD008420 (2014).

Biomedical Optics EXPRESS

81. M. Rodríguez-Calvo-de-Mora, R. Quilendrino, L. Ham, V. S. Liarakos, K. van Dijk, L. Baydoun, I. Dapena, S. Oellerich, and G. R. Melles, "Clinical outcome of 500 consecutive cases undergoing Descemet's membrane endothelial keratoplasty," Ophthalmology **122**(3), 464–470 (2015).
82. M. Rodriguez-Calvo-de-Mora, R. Quilendrino, L. Ham, V. S. Liarakos, K. van Dijk, L. Baydoun, I. Dapena, S. Oellerich, and G. R. Melles, "Clinical outcome of 500 consecutive cases undergoing Descemet's membrane endothelial keratoplasty," Ophthalmology **122**(3), 464–470 (2014).
83. A. Ćirković, U. Schlötzer-Schrehardt, J. M. Weller, F. E. Kruse, and T. Tourtas, "Clinical and ultrastructural characteristics of graft failure in DMEK: 1-year results after repeat DMEK," Cornea **34**(1), 11–17 (2015).
84. C. Monnereau, R. Quilendrino, I. Dapena, V. S. Liarakos, J. F. Alfonso, F. Arnalich-Montiel, M. Böhnke, N. C. Pereira, M. Dirisamer, J. Parker, K. Droutsas, G. Geerling, G. Gerten, H. Hashemi, A. Kobayashi, M. Naveiras, O. Oganesyan, E. Orduña Domingo, S. Priglinger, P. Stodulka, J. Torrano Silva, Jr., D. Venzano, J. M. Vetter, E. Yiu, and G. R. Melles, "Multicenter study of descemet membrane endothelial keratoplasty: first case series of 18 surgeons," JAMA Ophthalmol. **132**(10), 1192–1198 (2014).
85. T. Brockmann, C. Brockmann, A. K. Maier, J. Schroeter, U. Pleyer, E. Bertelmann, A. M. Joussen, and N. Torun, "Clinicopathology of graft detachment after Descemet's membrane endothelial keratoplasty," Acta Ophthalmol. **92**(7), e556–e561 (2014).
86. M. S. Gorovoy, "DMEK Complications," Cornea **33**(1), 101–104 (2014).
87. G. R. Melles, T. S. Ong, B. Ververs, and J. van der Wees, "Preliminary clinical results of Descemet membrane endothelial keratoplasty," Am. J. Ophthalmol. **145**(2), 222–227 (2008).
88. R. Y. Yeh, R. Quilendrino, F. U. Musa, V. S. Liarakos, I. Dapena, and G. R. Melles, "Predictive value of optical coherence tomography in graft attachment after Descemet's membrane endothelial keratoplasty," Ophthalmology **120**(2), 240–245 (2013).

1. Introduction

The integrity of the cornea and the ocular surface is essential for normal vision. Globally, corneal disease is a major cause of blindness including a wide variety of infectious, inflammatory and hereditary disorders [1, 2]. Clinically the cornea is examined using slit lamp biomicroscopy at various magnifications. Different lighting regimen such as diffuse illumination, focal illumination, indirect illumination and retroillumination can be used to further differentiate tissues and layers. To assess the shape of the cornea, keratoscopic techniques are available. Placido-disk based keratoscopy is based on looking into the reflected image from the corneal surface of an object composed of multiple discs. Nowadays videokeratoscope-based technology allows for identification of astigmatism, keratoconus, or corneal scars, but no information on the posterior surface of the cornea is obtained [3]. Slit-scanning elevation topography combines the principles of Placido-disk based keratoscopy with those of slit scanning providing measurements of anterior and posterior curvature as well as mapping the structure of the cornea [4]. Scheimpflug cameras use imaging where the plane of an object is not parallel to the film of the camera. Modern instruments employ rotating Scheimpflug cameras that take multiple slit-images and allow for quantification of corneal elevation, curvature, and thickness [5]. The standard technology for measuring corneal thickness is ultrasound pachymetry, by measuring the ultrasound propagation time in the tissue. Using very high frequency it is also possible to do multi-layered pachymetry [6].

The above-mentioned imaging techniques are, however, all limited by their resolution, which does not provide visualization of structures down to the microscopic range. Specular microscopy, introduced in the 1920s, is used to visualize the corneal endothelium interface and has integrated software capable of analyzing endothelial cell morphology and cell-count within a predetermined fixed frame [7]. Newer technology uses automatic image focusing, allowing pachymetric measurements. Imaging at a cellular level is also possible using confocal microscopy (CM) [8]. By applying the principles of confocal imaging it is possible to omit defocused light from reaching the detector. This increases optical resolution and contrast.

Soon after its first use for *in vivo* imaging of the human retina in 1993 [9], optical coherence tomography (OCT) was also applied to the anterior segment of the eye [10]. The advancements in acquisition speed and sensitivity that came along with the introduction of spectral-domain (SD) OCT allowed imaging of both the morphology of the cornea and the corneo-scleral limbus as well as the limbal microvasculature [11–15]. The advances in

Biomedical Optics EXPRESS

broadband light source technology led to axial resolutions of a few micrometers and enabled visualization of all distinct layers and morphological structures of the anterior eye segment *in vitro* [16] and *in vivo* [17–21]. The limbal palisades of Vogt, which are the putative location of the corneal stem cells, were imaged both, *ex vivo* and *in vivo*, using full-field optical coherence microscopy (FFOCM) [22] and ultrahigh-resolution OCT (UHR-OCT) [23, 24]. Using a broadband superluminescent diode spectrally centered at 1060 nm, images of nerve fiber bundles in the peripheral cornea as well as limbal and scleral lymph and blood vasculature in healthy eyes were also shown [24].

The high axial resolution of UHR-OCT systems allowed precise delineation of the corneal layers and together with the short recording times enabled measurement of epithelium and Bowman's layer thickness in both normal and keratoconic eyes [25, 26]. Using SD-OCT prototypes, pathologic changes in the Descemet's membrane in different stages of Fuchs' endothelial dystrophy could be visualized [27, 28].

While the axial resolution in OCT is inversely proportional to the bandwidth of the light source, the lateral resolution is determined by the diffraction limited spot size in the focal plane of the probe beam [29]. The minimum spot size is inversely proportional to the numerical aperture (NA) of the focusing optical system. In order to achieve a high lateral resolution, a large numerical aperture has to be used. The depth of focus, however, is inversely proportional to NA^2, thus, increasing the lateral resolution decreases the depth of field. Therefore, OCT is typically operated at low NA to allow a long depth of focus in the range of several hundred micrometers for imaging of biological tissues. This limits the lateral resolution to values in the range of 15 to 20 µm, hampering imaging on a cellular level. Using a liquid lens for dynamic focusing on different depth locations [30], Gabor-domain OCM allowed to overcome this limitation and provided non-contact *ex vivo* imaging of corneal cells in various layers and corneal nerves in the central cornea, comparable to CM [31].

Further fields of applications of the new developments in OCT technology are wide and range from biometry and pachymetry to evaluation of surgical outcome after e.g. treatment of anterior corneal scarring [32] or refractive surgery [33]. In addition, OCT might allow for localization of the demarcation line after cross-linking procedures in keratoconus [34].

Beside the imaging anterior segment's morphology and vasculature, UHR-OCT was shown to be capable of resolving the pre-corneal tear film [18, 35, 36] and to provide tear film thickness maps [37] of the central cornea, which gives the technology a potential for diagnosis and treatment monitoring in dry eye diseases [38, 39]. Furthermore, the assessment of the OCT reflectance provided super-resolved visualization of the tear film lipid layer [40].

In the present paper, we show images of various corneal pathologies taken by a custom-built ultrahigh-resolution OCT system with a resolution of approximately 1.2 µm and discuss possible implications for the use of this device in clinical practice.

2. Methods

2.1. Ultrahigh-resolution OCT

The experimental setup used for *in vivo* high-resolution imaging of the anterior eye segment is an adapted version of the ultrahigh-resolution SD-OCT system for imaging of the human precorneal tear film and has been reported previously [35]. The setup is based on a broad bandwidth Ti:sapphire laser (Integral OCT; Femtolasers Produktions GmbH, Vienna, Austria) with a spectrum centered at 800 nm. The full width at half maximum (FWHM) bandwidth of the source is 170 nm, which results in a theoretical axial resolution of 1.2 to 1.3 micrometers, depending on the measured tissue structures. The optical system was designed in order to deliver optimal performance for broad spectral bandwidth used for imaging. The free space Michelson interferometer is built up by a beam splitter plate (BSN17, Thorlabs GmbH, Dachau/Munich, Germany) with an asymmetric splitting ratio of 90:10 and contains two variable neutral density (ND) filters. The first one at the input of the interferometer allows to set the probe beam power according to the maximum permissible exposure (MPE) limits as

Biomedical Optics EXPRESS

specified by the International Electrotechnical Commission (IEC 60825-1) [41] and by the American National Standard for Safe Use of Lasers (ANSI Z136.1) [42] and to optimize the signal that arises from the sample and is detect by the spectrometers CCD camera. The second ND filter in the reference arm is used for balancing the reference arm signal according to the reflectivity of the sample. In addition, a prism pair is used for compensating the group velocity dispersion (GVD) mismatch caused by the optics in the sample arm. The sample arm comprises a two-axis galvanometric scanner (GVS002; Thorlabs GmbH) for directing and an OCT scan lens objective (LSM04-BB; Thorlabs GmbH) for focusing the probe beam onto the sample. Taking the parameters of the probe beam and the focal length of the imaging optics into account yields a lateral resolution of 20 µm at the sample. Two achromatic fiber collimators (f = 12 mm, Schäfter Kirchhoff GmbH, Hamburg, Germany) are used to collimate the input light emitted by the light source and to couple the light from the exit of the interferometer. This spectral signal is then directed towards a custom built spectrometer. The spectrometer is composed of a collimator with focal length f = 100 mm (OZ Optics, Ottawa, Canada) and a holographic transmission diffraction grating with 1200 lines per mm (Wasatch Photonics, Logan, UT, USA). The light emerging from the grating is imaged by means of an objective with a focal length f = 85 mm (ZEISS PLANAR T 1.4, ZF-IR-I; Carl Zeiss AG, Oberkochen, Germany) onto a high-speed line array CCD camera (Basler sprint spL4096-140km; Basler AG, Ahrensburg, Germany) with 4096 pixels and maximum readout rate of 140 kHz. As compared to the previously presented version two changes regarding the spectrometer part of the system were done: Firstly, the maximum acquisition speed increased from 70 000 to 140 000 A-scans per second, leading to a shortening of the recording time thereby reducing the effect of involuntary eye movements. Secondly, the depth range of the UHR-OCT system was almost doubled (z = 2 mm), allowing imaging of the junction zone between cornea and limbus with higher lateral scanning ranges. The signal-to-noise ratio close to the zero delay was measured with 97 dB (1.5 mW probe beam power) and the sensitivity decay due to the finite spectrometer resolution is 10 dB to a depth of 1 mm. The data acquisition and visualization is done in Labview (Labview 2013, National Instruments, Austin, TX, USA), while the post processing is performed in MATLAB (MATLAB R2013b, The MathWorks Inc., Natick, MA, USA).

For human *in vivo* measurements, the optical power incident on the subject's anterior segment structures is set to values between 1 and 2 mW, depending on the tissue to be probed. However, all exposure values are well below the MPE of 8.6 mW for the current configuration as specified by [41, 42], to ensure the safety of the eye.

2.2. Data collection and processing

UHR-OCT tomograms and three-dimensional data sets were acquired *in vivo* from both healthy subjects and patients with various pathologies of the corneal or limbal region. All imaging procedures were approved by the Ethics Committee of the Medical University of Vienna. The nature of the measurements was explained to all participating subjects and written consent to participate was given. The protocol of the study complied with the standards of the Declaration of Helsinki.

Before OCT measurements, subjects underwent a screening examination including slit lamp biomicroscopy and assessment of medical history. For the measurement procedure, the head of the subject was stabilized on a modified slit lamp head rest, and the subject was advised to fixate either an internal fixation target for corneal imaging or an external target for probing of structures of the limbal area. Both scanning range of the XY-galvanometric scanner and the sampling density of the tomograms and volume data sets were individually adapted for optimal visualization of the anterior eye segment structure of interest. All images comprised 2048 pixels in depth, corresponding to about 1.5 mm in tissue. Measurement times varied between one and seven seconds, depending on the targeted sampling density. Motion artifacts in between the acquired tomograms caused by involuntary eye movements of the

Biomedical Optics EXPRESS

subject were compensated based on cross-correlation of consecutive images [43]. For calculation of corneal thicknesses, group refractive indices for stroma and epithelium of 1.38 [44] and 1.40 [45] were assumed.

3. Results

3.1. Healthy cornea

Figure 1 shows a representative cross-sectional UHR-OCT image of a healthy human cornea. All major corneal layers, including epithelium (EP), Bowman's layer (BL), stroma (ST), Descemet's membrane (DM) and corneal endothelium (ED) can be distinguished. Furthermore, the precorneal tear film (TF) – seen as the topmost highly reflective layer in the tomogram – can be visualized. From Fig. 1 it is also worth noting that at the interface between epithelium and Bowman's layer, epithelial tissue shows lower reflectivity (darker appearance in the tomogram) compared to the overlying epithelial layers.

The appearance in the tomogram reflects well the morphology of this corneal layer. Briefly, the epithelium consists of five to six layers of cells with a total thickness of approximately 50 µm. At the base, a single layer of columnar shaped cells with a height of 15 to 20 µm is found. This layer is followed by two to three layers of wing cells. Most superficially, two layers of squamous cells with flattened nuclei can be found. As compared to the overlying cell layers, the basal epithelial cells have a low nucleus-cytoplasm ratio [46, 47]. Furthermore, while superficial epithelial cells show hyperreflective nuclei, basal epithelial cells appear hyporeflective and have only hyperreflective borders [48, 49]. Taking into account their columnar shape oriented "in parallel" to the incident probe beam and the fact that it consist of only one layer of cells, this explains the lower scattering of the basal layer of epithelium (BLE).

Based on the three-dimensional UHR-OCT data set of the healthy subject, average thicknesses of the corneal layers were measured as follows: central cornea 585 µm, epithelium 55 µm, Bowman's layer 18 µm, Descemet's membrane 10 µm and endothelium 4.5 µm.

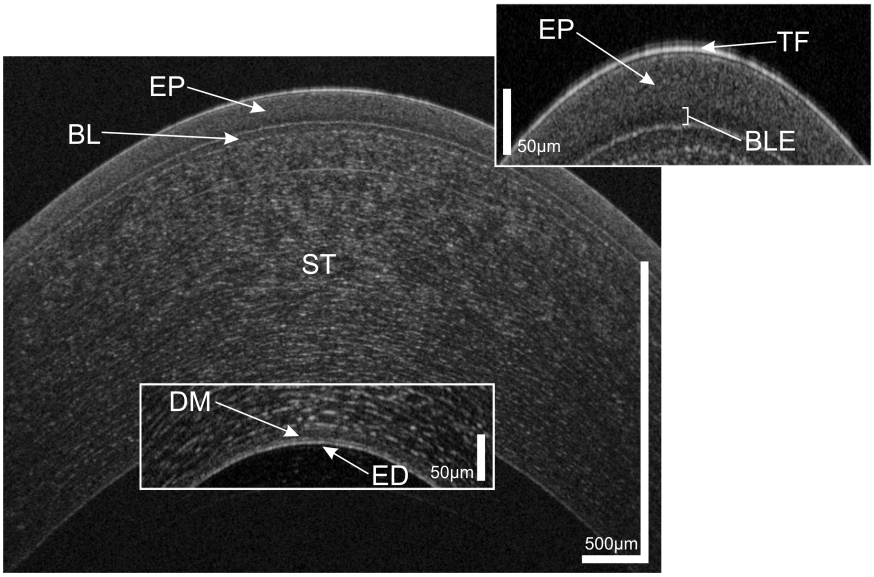

Fig. 1. UHR-OCT tomogram of the central and paracentral zone of the cornea of a 38 year old healthy male. TF, tear film; EP, epithelium; BLE, basal layer of epithelium; BL, Bowman's layer; ST, corneal stroma; DM, Descemet's membrane; ED, endothelium.

Biomedical Optics EXPRESS

High resolution imaging of the limbal palisades of Vogt is shown in Fig. 2. The palisades of Vogt are a series of radially oriented fibrovascular ridges in the limbus that cross this junctional zone between the cornea and conjunctiva [50, 51]. Corneal epithelial stem cells are thought to reside at this region of the corneal limbus, mainly superiorly and inferiorly.

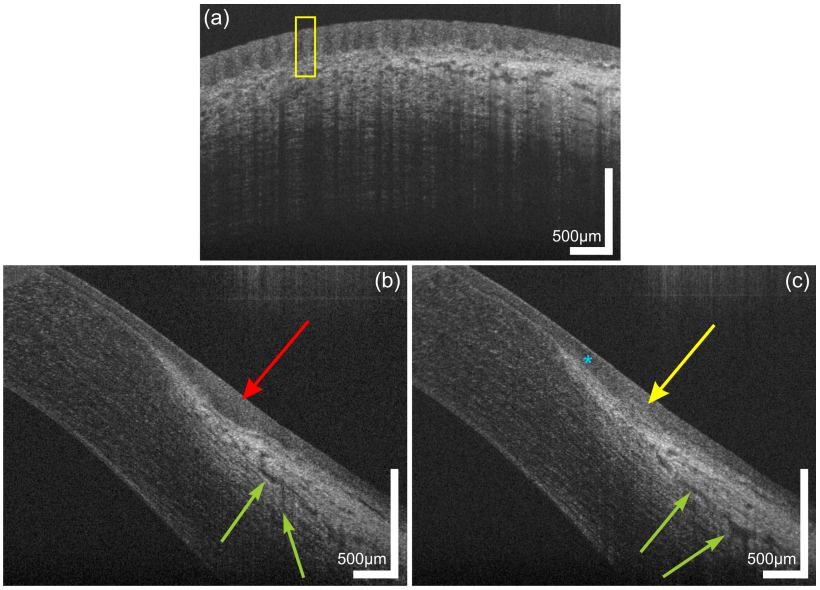

Fig. 2. Limbal palisades of Vogt of a 38 year old male subject. (a) Transversal scan at the inferior limbus revealing the fence-like structure of the palisades with highly reflective collagen ridges. (b,c) Sagital scans at (b) inter-palisade and (c) palisade positions yielding the difference in reflectivity at the putative location of the stem cell niches. The blue asterisk indicates the hyperreflective extension of the corneo-scleral junction. Green arrows indicate parts of the conventional aqueous humor drainage pathway.

Multiple stacks of UHR-OCT images were acquired at the inferior limbus of a healthy subject. Exemplary tomograms with different orientations of the fast axis of the probe beam scanner are depicted in Fig. 2. In the transversal scan presented in Fig. 2(a), limbal palisades of Vogt appear as a fence-like structure, yielding different scattering properties within this region. The yellow rectangle indicates the stronger scattering collagen ridges of the palisades with regions of reduced scattering in-between. In Figs. 2(b) and 2(c), sagittal scans of the same region are shown. The red arrow in Fig. 2(b) indicates the low scattering region while the yellow arrow in Fig. 2(c) reveals again the highly scattering collagen ridges corresponding to the putative location of the limbal stem cell niches. Furthermore, a hyper-reflective band (blue asterisk) is visible in the transition zone between corneal epithelium and conjunctiva. The power of the probe beam was adjusted in order to allow optimal visualization of the superficial structures of the limbus, avoiding saturation of the CCD camera by highly reflective structures of the sclera. Therefore, visibility of deeper limbal structures is reduced. However, still some features of the aqueous outflow system can be visualized. Aqueous humor is drained by collector channels, directly via aqueous veins or indirectly via intrascleral plexus towards episcleral veins. The green arrows exemplary indicate intrascleral plexus and episclearal plexus, both part of the conventional drainage pathway.

Three-dimensional UHR-OCT data sets were acquired at the temporal cornea and limbal transitional zone to the sclera of a healthy subject. Again all corneal layers are clearly visualized (Fig. 3). The right side of the image shows the highly reflective limbal structures of blood vessels (red asterisk) casting shadows due to the light absorption of blood and two layers of aqueous venous plexus (green arrows).

Biomedical Optics EXPRESS

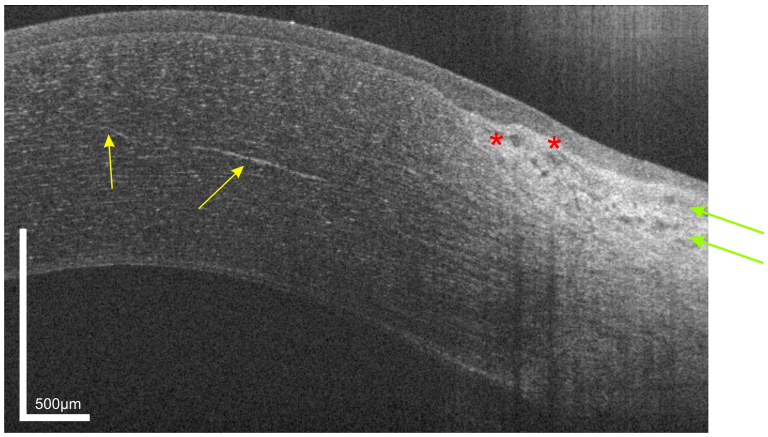

Fig. 3. UHR-OCT tomogram of the paracentral and peripheral cornea and limbus of the same subject as in Fig. 1. In the mid stroma, a highly reflective corneal nerve (yellow arrows) with a thickness between 5µm (central) and 10 µm (paracentral) is visible. In the limbus, blood vessels (red asterisk) as well as conjunctival and episclearal plexus (green arrows) are shown.

In the mid stroma, a highly reflective structure with a thickness decreasing from the peripheral (10µm) to the paracentral-central (5 µm) cornea can be visualized. This structure most probably corresponds to a corneal nerve fiber bundle. The nerve bundles enter the cornea at the periphery in a radial manner. Within approximately 1 mm of the limbus, nerve bundles lose their perineurium and myelin sheaths [52] to maintain corneal transparency. After that they continue only surrounded by Schwann cell sheaths and further subdivide into smaller side branches. This change in ultrastructure reduces the ability of OCT to visualize corneal nerves in the central zone.

3.2. Corneal pathologies

3.2.1. Traumatic corneal injuries

3.2.1.1. Corneal abrasion

Figure 4 depicts a high resolution OCT scan of a corneal epithelial defect. In Fig. 4(a), a slit lamp photography using Fluorescein staining to mark the corneal erosion four days after accelerated epi-off CXL is shown. Clearly, the epithelial defect in the central cornea is visible. UHR-OCT volume data, comprising 1024 x 512 x 2048 pixels corresponding to 7.5 x 7.5 x 1.5 mm (horizontal x vertical x depth), were acquired [34]. In the cross-sectional image depicted in Fig. 4(b), the epithelial erosion can clearly be observed. Four days after corneal abrasion, wound healing was far advanced. Only in the central region close to the apex of the cornea, the depth of the wound still approximated Bowman's layer. Only this area of the wound was stained by fluorescein. This region could be easily identified in the tomogram. In addition, in the paracentral zone of the cornea the OCT images show some more superficial irregularities in the epithelium, indicating that the epithelium surrounding the fluorescein stained abrasion is not fully settled as the cells consolidate their attachments to the underlying basement membrane.

Biomedical Optics EXPRESS

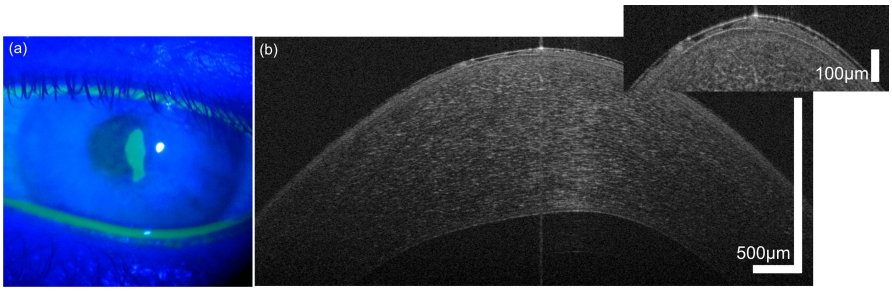

Fig. 4. Corneal epithelial abrasion in a 25 year old male with progressive keratoconus, image taken 4 days after epi-off corneal collagen cross-linking procedure. (a) slit lamp photograph with Fluorescein staining showing the defect, (b) corresponding OCT image.

3.2.1.2. Intrastromal foreign body

Figure 5 shows an OCT (a) and slit lamp image (b) of an intracorneal foreign body obtained four days after an accident of a spectacle wearer. Using the UHR-OCT image, the exact position of the intracorneal foreign body can be determined. The strong reflectivity points to glass debris in the anterior stoma. The cut in stroma involving different reflectivity values and shadowing effects in the OCT signal is clearly visible, while the epithelial wound is already closed. However, UHR-OCT reveals a displacement of the wound margin as well as a small corneal flap consisting of epithelial and stromal tissue.

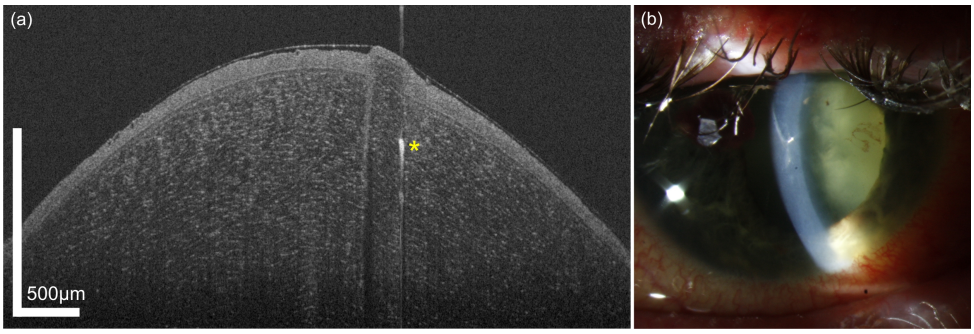

Fig. 5. Intrastromal foreign body in a 43 year old male patient who wore glasses during an accident. The injury was accompanied by a globe perforation. During the slit lamp examination after surgery, a corneal foreign body was noted; yet, it was not clear whether it needed immediate removal through a second surgical intervention or not. (a) OCT image, (b) slit lamp photograph.

3.2.1.3. Chemical burn

The patient in Fig. 6 suffered from an alkali burn ten years ago. Figure 6(a) shows the slit lamp photograph of the patient, in which corneal neovascularization has developed. UHR-OCT three-dimensional data sets were acquired on the temporal limbus of both the healthy right eye and the affected left eye. Comparison of the images demonstrates several differences. Firstly, a significant thinning of the peripheral cornea is observed. While the thickness of the healthy cornea in the periphery close to the limbus was measured at 635 µm, the similar location of the diseased eye had a thickness of 401 µm.

Biomedical Optics EXPRESS

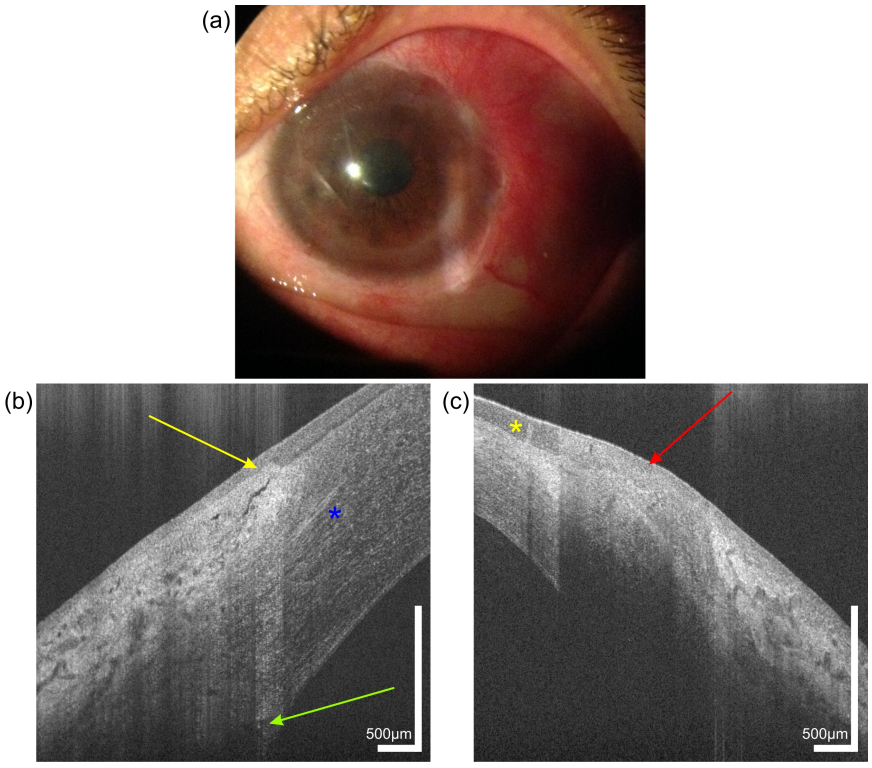

Fig. 6. Image of a 44 year old female patient with a chemical burn in her left eye, caused by a bathroom cleaner 10 years ago. Slit lamp photography (a) of the left eye reveals corneal neovacularization. UHR-OCT cross-sectional images of the temporal limbus of the (b) right and (c) left eye. Yellow arrow, limbal palisade of Vogt. Red arrow, scar tissue with absence of palisades. Yellow asterisk indicates the position of a newly formed vessel in the conjunctiva. Green arrow, Schlemm's canal. Blue asterisk, corneal nerve.

Furthermore, UHR-OCT revealed significant differences in the limbal palisades of Vogt when comparing the healthy (b) with the injured eye (c) of the patient. The absence of the clear differentiation of limbal tissue structures with the palisades of Vogt (yellow arrow in Fig. 6(b)) indicates stem cell deficiency. The high absorption of the probe beam light by the scar tissue (red arrow in Fig. 6(c)) prevents visualization of deeper limbal structures. In addition, OCT scans of the wounded eye reveal neovascularization in the transition zone between epithelium and limbus (yellow asterisk) with a blood vessel casting a shadow due to the light absorption of red blood cells. Despite the low probe beam power used for imaging of superficial tissues, the sensitivity in the deeper layers is high enough to visualize Schlemm's canal in the limbus of the healthy eye (green arrow in Fig. 6(b)). In addition, in the mid stroma corneal nerve (blue asterisk) is visible.

3.2.2. Corneal inflammatory and infectious diseases

3.2.2.1. Acanthamoeba keratitis

Acanthamoeba is a free-living protozoa with two phases in its life cycle: firstly, the active trophozoite form and, secondly, the double walled cyst, which is resistant to treatment. The resistance in the second phase is mainly due to cellulose molecules present in the inner layer of the cysts. This cellulose double coating is the main source of scattering used for optical imaging modalities like OCT and confocal microscopy.

Figure 7(a) shows an *in vivo* confocal microscopy image of a patient with Acanthamoeba keratitis. Here, Acanthamoeba cysts present themselves as highly reflective structures in the

Biomedical Optics EXPRESS

central part of the image. Figure 7(b) and 7(c) show the same patient examined with UHR-OCT in the same location on the cornea. In the magnified cross-sectional image (c), at least three highly reflective dots indicating the presence of cysts in the anterior third of the cornea can be seen. In addition, the defects in the epithelium and the anterior stroma are clearly visible.

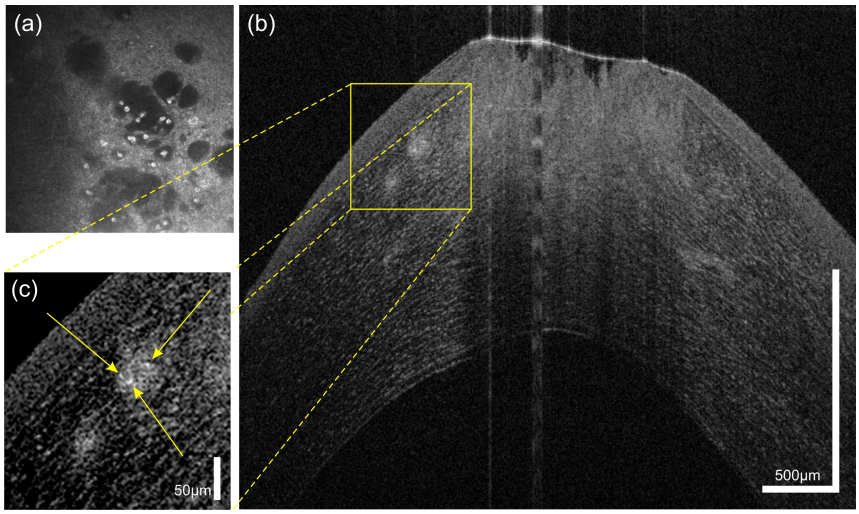

Fig. 7. 45 year old male patient with Acanthamoeba keratitis, (a) Confocal microscopy depicting Acanthamoeba cysts. (b) and (c) UHR-OCT scans of the same patient revealing at least three cysts (yellow arrows) and defects in epithelium and anterior stroma.

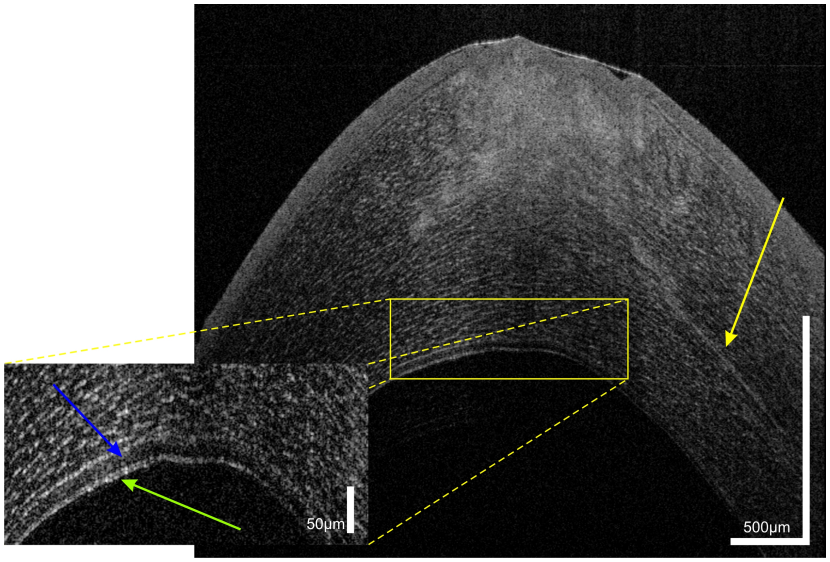

Fig. 8. UHR-OCT of Acanthamoeba keratitis in the same patient as shown in Fig. 7. The cross-sectional image reveals radial keratoneuritis with a thickened corneal nerve and a hyporeflective space (blue arrow) above the double banded structure of the epithelium.

The UHR-OCT image in Fig. 8 was obtained at another vertical position within the three-dimensional OCT data and revealed radial keratoneuritis (yellow arrow), which is an inflammatory response of the corneal nerves and is associated with a perineural infiltrative process. In the OCT scan it presented as thickening of the corneal nerve in the mid stroma when compared to the healthy state in Fig. 3. Furthermore, the borders of the nerve appear

Biomedical Optics EXPRESS

rugged. In addition, UHR-OCT also reveals a hyporeflective space (blue arrow) in the anterior cornea with several reflective particles in it. Since the Descemet's membrane is the basement membrane of the endothelium (green arrow), a separation of the two layers is extremely unlikely. The double banded appearance of the most inferior structure in the tomogram with the hyporeflective space above might therefore correspond to a split in Descemet's membrane with a mixture of fluid and collagenous material in it.

3.2.2.2. Herpetic keratitis

In Fig. 9, image data of a 34 year old patient with sequelae after herpes keratitis infection are shown. The slit lamp photography in Fig. 9(a) reveals corneal haze and neovascularization. UHR-OCT three-dimensional data sets covering a region of 7 mm x 7 mm x 1.5 mm and containing 650 x 650 x 2048 pixels were acquired at the central and paracentral zone of the cornea. All distinct corneal layers (EP, BL, BLE, ST, DM, ED) could again be visualized. Measurement of corneal thickness yielded a significant thinning of the affected part of the cornea (average thickness 377 µm) as compared to the healthy eye (581 µm). A cross-sectional image obtained at the location marked in the slit lamp photography is depicted in Fig. 9(b). In the deep stroma, highly reflective condensed tissue due to scarring with presence of calcification and lipid is seen as single highly reflective scattering zone. In addition, extensive corneal neovascularization is present, which can be clearly seen in the OCT image.

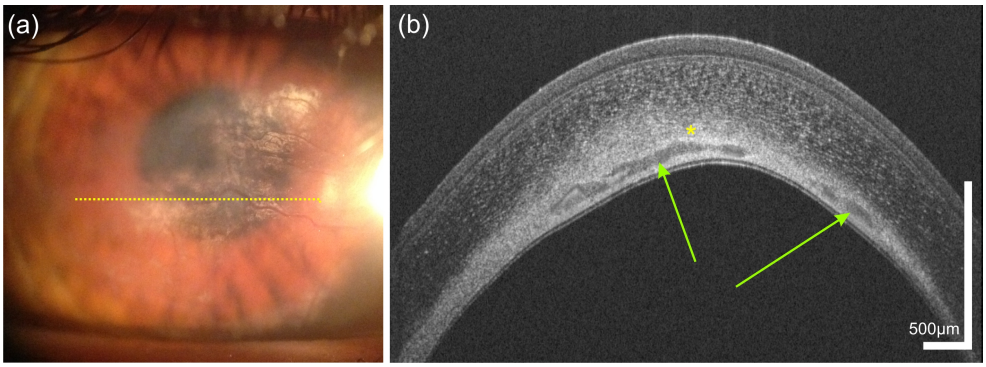

Fig. 9. Sequelae after herpetic keratitis in a 34 year old male who was first diagnosed 3 years ago. The slit lamp photography (a) as well as the OCT image (b) reveal neovascularization. Yellow dotted line in (a) indicates the location of the UHR-OCT scan; Green arrows, corneal neovascularization; yellow asterisk, calcifications/lipid.

3.2.3. Corneal dystrophies

3.2.3.1. Keratoconus

Keratoconus is a progressive non-inflammatory disease of the cornea, leading to thinning and gradual protrusion of the cornea. Corneal ectasia can result in high myopic astigmatism and irregular astigmatism and thereby to severe visual distortion [53, 54].

A three-dimensional data set covering a 512 x 512 x 2048 pixels and 7 mm x 7 mm x 1.5 mm of the central and paracentral cornea of a patient with progressive keratoconus scheduled for epi-off corneal collagen cross-linking (CXL) was acquired. In Fig. 10, an UHR-OCT image close to the corneal apex is depicted. While Scheimpflug imaging (Pentacam HR, OCULUS Pentacam, Wetzlar, Germany) only allowed depicting the central corneal thickness in general (491 µm in the presented patient), UHR-OCT enabled assessment of both corneal and epithelial thickness in the central and paracentral zone of the cornea. OCT measurement of corneal thickness yielded a value of 505 µm. In addition, the cross-sectional image revealed the typical thinning of the epithelium in the left paracentral zone and compensatory thickening in the opposing zone of the cornea.

Biomedical Optics EXPRESS

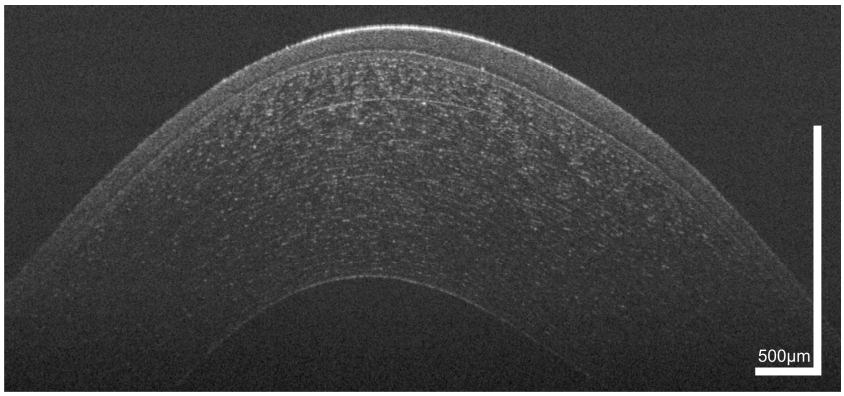

Fig. 10. Cross sectional image of the paracentral zone of the cornea of a 38 year old male patient with progressive keratoconus. Epithelial thinning in the paracentral cornea is visualized.

In Fig. 11(a), a Scheimpflug tomography map of corneal refractive power is shown. The region of highest refractive power corresponding to the thinnest zone of the cornea is found in the temporal inferior part of the cornea. In Fig. 11(b), an epithelial thickness map extracted from the OCT volume data and corrected for corneal curvature and incident angle of the probe beam is depicted. As can be seen, the location of the thinnest zone of the epithelium evaluated via UHR-OCT corresponds very well with the steepest zone of the cornea extracted by Scheimpflug tomography.

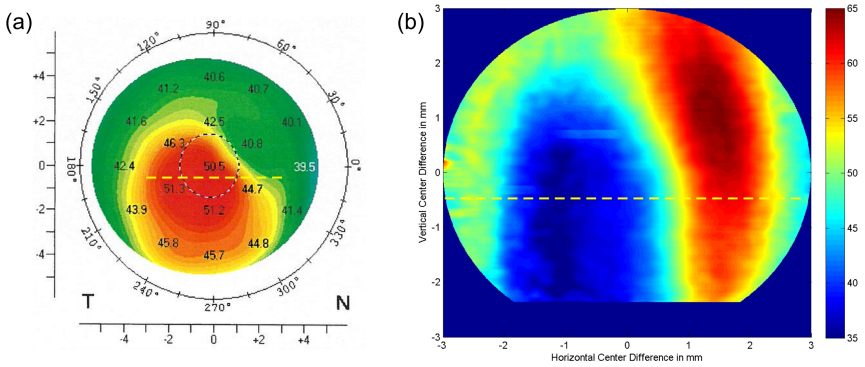

Fig. 11. Corneal topography of the same 38 year old patient as shown in Fig. 10. (a) Corneal refractive power as measured via Scheimpflug tomography. (b) Epithelial thickness map retrieved from a three-dimensional UHR-OCT data set. Yellow dashed lines in both figures indicate the position of the cross-sectional scan depicted in Fig. 11. Due to reduced signal-to-noise-ratio in the periphery, the evaluated region was cropped to a circular pattern with a diameter of 6 mm. The thinnest region of the cornea is present in the temporal inferior part and corresponds well with the thinnest zone of the epithelium as measured by UHR-OCT.

3.2.3.2. Fuchs' endothelial dystrophy

Fuchs' endothelial dystrophy is the most common posterior corneal dystrophy [55]. It is characterized by a non-inflammatory, bilateral slowly progressing degeneration of endothelial cells, eventually leading to corneal decompensation and visual decline.

In Fig. 12, a case of early stage Fuchs' endothelial dystrophy is presented. The guttatae in the endothelium are clearly visible in the OCT image (a), even though the slit lamp photograph shows scarce details (b). Furthermore, a thickening of DM with an average thickness of 24.5 µm was observed.

Biomedical Optics EXPRESS

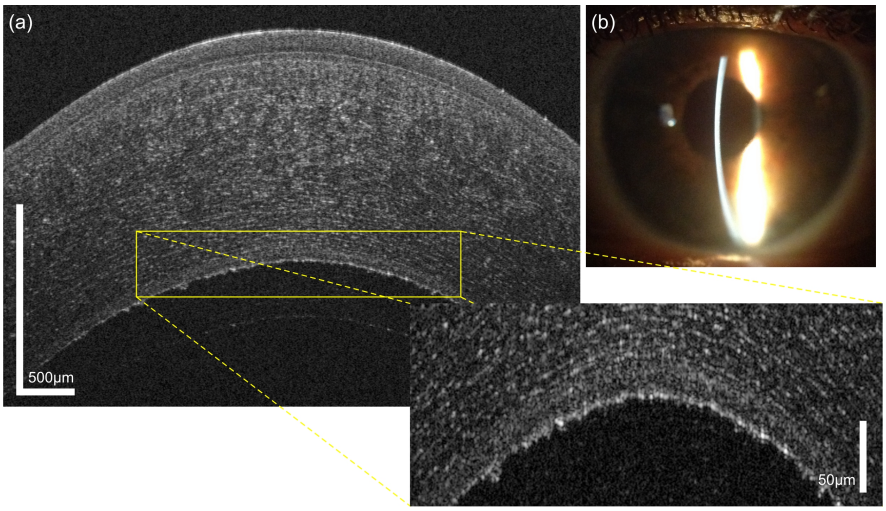

Fig. 12. Fuchs' endothelial dystrophy that was newly diagnosed in a 60 year old female patient, (a) OCT image, (b) corresponding slit lamp photograph.

Figure 13 shows a patient with Fuchs' dystrophy in an advanced stage after Descemet's membrane endothelial keratoplasty (DMEK). The endothelial graft can be visualized well; in addition, a small area with an irregularity in the recipient stroma bed with retained interface fluid (yellow arrow) can be observed.

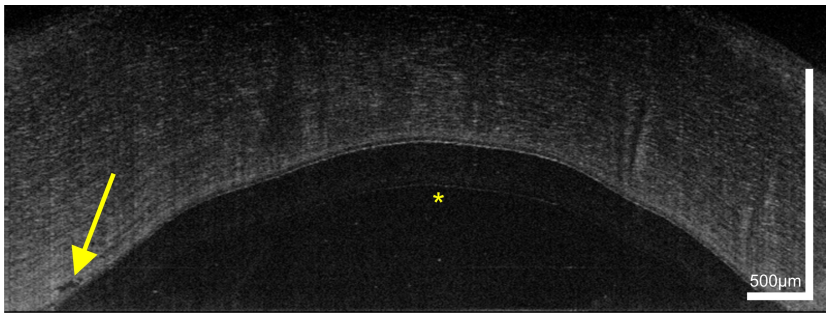

Fig. 13. UHR-OCT image of the cornea of a 74 year old female patient who underwent DMEK for Fuchs' dystrophy (24 hours postoperatively). Yellow arrow marks an irregularity in the recipient stroma. Yellow asterisk indicates an image artifact due to the internal fixation target of the OCT.

4. Discussion

In this report we present the potential of UHR-OCT with a theoretical axial resolution of 1.2 µm in air to image corneal pathologies. The technique may have considerable potential for improved clinical decision making and treatment monitoring.

The cornea consists of five distinct layers that can all easily be identified on the presented OCT images (Fig. 1). Using this approach we were able to obtain average thickness of epithelium, Bowman's layer, stroma and Descemet's membrane in healthy subjects. In contrast to commercial systems, we were also able to distinguish endothelium from Descemet's membrane. Recently, an UHR-OCT prototype based on a supercontinuum laser as light source has been presented allowing *in vivo* imaging and thickness measurements of the human Pre-Descemet's layer and endothelium [56].

We have further presented images of human stem cell niches located in the limbal palisades of Vogt (Fig. 2). Epithelial stem cells are situated within well-defined niches called limbal epithelial crypts [57, 58]. These cells are responsible for the self-renewal capacity of

Biomedical Optics EXPRESS

the epithelium and ensure maintenance of epithelial turn over in the normal cornea. Imaging of these structures has been provided previously using OCT, but with lower resolution than in the present study [59].

Furthermore, corneal fine structures, such as corneal nerves, can be visualized using this technique (Fig. 3). This may be useful in systemic diseases associated with neuropathy, such as diabetes mellitus, but also in ocular diseases such as infectious keratitis, corneal dystrophies, and neurotrophic keratopathies. In addition, visualization of corneal nerves after refractive surgery might be of interest [60]. An advantage of this technique over CM is the contact-free nature of OCT. However, a quantitative parameter for assessing and monitoring corneal nerves with OCT has yet to be determined.

As epithelium can be visualized using ultrahigh resolution OCT, wound healing rates as measured with the device allow for evaluation of treatment effects following pharmaceutical interventions [34]. Figure 4 provides an example of an epithelial defect. It is clearly visible that the tear film covers this defect. Indeed, the role of tear film maintenance of tissue homeostasis and wound healing is not fully understood. It is, however, well established that epidermal growth factor release rates are significantly lower in patients undergoing corneal wound healing than in normal eyes during reflex tearing [61].

Figure 5 shows a case of an intracorneal foreign body. OCT offers advantages over other imaging technologies because it is easy to determine whether DM is penetrated or not. By identifying the exact location, the optical properties of the intracorneal foreign body and the status of the surrounding ocular structure, the OCT imaging provides guidance for the choice of timing and the selection and planning of the optimal surgical technique. In this case, no surgery was necessary since the high reflectivity suggested a remnant glass fragment in the stroma from the patient's spectacles. Since glass is considered to be completely inert, no immediate removal was required [62]. However, because complications such as keratopathy or irregular astigmatism may occur, the patient has to be followed up regularly [63, 64].

UHR-OCT was employed for visualization of an alkali burn in the eye as depicted in Fig. 6. Corneal neovascularization is clearly visible and a result of limbal stem cell deficiency that is often associated with the chemical injury [65, 66]. When looking at the stem cell niches of this patient, morphological differences between the healthy right eye and the injured left eye can be clearly seen. Autologous Simple Limbal Epithelial Transplantation (SLET) is a relatively new approach for treatment of unilateral limbal stem cell deficiency that does not require sophisticated and expensive laboratory procedures for harvesting and expanding stem cells *in vitro*. In a single procedure, limbal tissue is removed from the healthy eye and distributed evenly over an amniotic membrane, which is then placed on the cornea of the diseased eye [67, 68]. In these cases, OCT of the limbal stem cell niche could be used for identifying the ideal site for harvesting limbal tissue and for assessment of long-term effects of the procedure on the donor site.

Acanthamoeba keratitis is a rare but sight-threatening inflammation of the cornea which is predominantly seen in patients wearing soft contact lenses. As Acanthamoeba occur ubiquitously in tap water, air and soil, they easily get into lens storage cases where they feed on other microorganisms. The life cycle of Acanthamoeba consists of two stages: the trophozoite stage, in which the organism feeds and multiplies, and the metabolically inactive cyst stage, which is induced in response to adverse environmental conditions and that enables the organism to withstand heat, UV radiation, biocides and chlorination. This explains why the infection is notoriously difficult to treat. Differential diagnosis is difficult and cultures from corneal scrapings have little sensitivity 30-70% [69]. Cysts can be visualized using confocal microscopy [70–72], helping to decide on the treatment regimen, which in itself is toxic to the limbal stem cells. However, the technique is contractile and only a limited field can be observed. Previously, high-resolution OCT allowed for *in vitro* imaging of cysts [73]. In the case presented in Figs. 7 and 8, Acanthamoeba cysts could, to the best of our knowledge, for the first time visualized *in vivo* using UHR-OCT although further studies are

Biomedical Optics EXPRESS

required to verify the clinical utility of this approach. In addition, the employed OCT system provided detailed visualization of radial keratoneuritis in the patient, a capability that may be helpful for diagnosis and follow-up in early stages of the disease.

In Fig. 9 corneal scarring after herpetic keratitis is shown. At the time when the measurement was performed, no inflammation was present. One can, however, see that there is a massive corneal thinning as a result of recurrent inflammation episodes that require treatment with corticosteroids. OCT can be useful in the follow-up of this patient, to precisely assess the stage of the disease, localization and extent of stromal scarring and neovascularization.

Visualization of the epithelium is not only interesting in patients with epithelial defects as presented above. Quantification of epithelial thickness is also valuable in keratoconus, a progressive disease leading to central corneal thinning, ectasia and irregular astigmatism (Figs. 10 and 11). Corneal collagen cross-linking is widely used to slow down or arrest progression of the disease [74]. Briefly, during this procedure the corneal epithelium is removed and riboflavin eye drops are applied for a pre-defined time-period followed by corneal exposure to ultraviolet A (UVA) light. This induces a photochemical reaction leading to an increase in cross-linking of the extracellular matrix and thereby to an increase in corneal rigidity [75]. Since CXL is used to prevent progression of keratoconus, patients at risk should be identified as early as possible. Data from several studies indicate that epithelial thinning precedes other corneal changes in keratoconus [76, 77]. Therefore, the use of UHR-OCT in these cases could be valuable for identifying those who should be treated. In addition, epithelial thickness measurements might also be interesting for the pre-operative screening in refractive surgery, to identify patients at risk for postoperative corneal ectasia. High-resolution epithelial thickness maps could also be employed for treatment planning in excimer-laser surgery of superficial scarring (phototherapeutic keratectomy).

In Fig. 12, an early case of Fuchs' endothelial dystrophy is shown. The measured increase in thickness of DM corresponds well with values previously obtained using UHR-OCT technology [27]. Corneal dystrophies are inherited disorders by inborn defects of cells associated with pathological changes leading to corneal haze [78]. Fuchs' dystrophy is a slowly progressive disease characterized by four stages: cornea guttata, endothelial decompensation, bullous keratopathy and stage of scarring. Ultrahigh resolution OCT may be an attractive approach to screen for the disease at an early stage which is of special importance when planning cataract surgery. During the surgical procedure, care has to be taken to avoid endothelial cell loss in these patients. This can be done by reducing the duration of surgery, avoiding direct endothelial trauma and using the proper viscoelastic material [79]. Since in Fuchs' endothelial dystrophy, except for the stage III, not all corneal layers are affected, less invasive surgical techniques such as Descemet's membrane endothelial keratoplasty (DMEK) have been developed. Treatment in Fuchs' endothelial dystrophy can be modulated according to the severity of the disease. While in PKP a full thickness piece of variable diameter of the patient's cornea is removed and then replaced by a corneal transplant from a donor's eye [80], DMEK only requires the replacement of a lamella consisting of Descemet's membrane and endothelium. After DMEK, the literature reports a re-surgery rate of approximately 5%, caused by graft failure or detachment [81–83]. Graft detachment has been identified as the main complication following DMEK occurring in up to 40% of patients after surgery [84, 85]. Some surgeons treat this complication by inserting air in the anterior chamber ("rebubbling") in order to achieve reattachment of the graft. The results of these procedures differ in the literature, since some authors report a failure rate requiring re-grafting in nearly 100% of patients [86, 87] while others report graft failure in 20% only [84]. Rebubbling has to be performed within the first six weeks after initial surgery since beyond that time the tissue becomes too rigid [88]. Figure 13 shows the cornea of a patient with Fuch's dystrophy after DMEK. The graft can be visualized well, allowing UHR-

Biomedical Optics EXPRESS

OCT to be used for monitoring of success of the intervention and the follow-up of patients after surgery.

5. Conclusion

In this paper we presented OCT imaging of the human cornea with a resolution of approximately 1.2 µm. The potential applications of this technology are wide, including quantification of tear film and its dynamics in patients with dry eye disease, OCT-guided refractive surgery, monitoring of epithelial wound healing, visualization of demarcation line after cross-linking in keratoconus and visualization of endothelial cell layer. Optimized scanning patterns and alternative illumination pathways may allow for improved peripheral imaging and improved transversal resolution, respectively.

In the presented pathologies, UHR-OCT has potential in clinical decision making and follow-up. Ultrahigh-resolution OCT of the cornea is not only a promising technique for the use in clinical practice, but may also be employed to gain novel insight into the physiology and pathophysiology of the human cornea and limbus.

Funding

Austrian Federal Ministry of Economy, Family and Youth, National Foundation of Research, Technology and Development; Heidelberg Engineering Academy Glaucoma Research Initiative; Hochschuljubiläumsstiftung der Stadt Wien (Project No. H-289408/2013). Dr. Sabina Sapeta has received an EVER (European Association for Vision and Eye Research) research fellowship.